Shallow Crustal Structure of the Tanlu Fault Zone Near Chao Lake in Eastern China by Direct Surface Wave Tomography from Local Dense Array Ambient Noise Analysis

NING GU,[1] KANGDONG WANG,[1,2] JI GAO,[1] NING DING,[3] HUAJIAN YAO,[1,4] and HAIJIANG ZHANG[1]

Abstract—Ambient noise tomography (ANT) has been used successfully to image shallow earth structure. Here we perform ANT on a local dense seismic array around the Tanlu fault zone (TFZ) to the southeast of Hefei City, Anhui Province in eastern China. The array consists of 53 stations with average spacing close to 5 km. Cross-correlations of vertical-component ambient noise data of different station pairs are computed in 1-h segments and stacked over 1 month from 17 March to 26 April 2017. Clear fundamental-mode Rayleigh waves are observed between 0.2 and 5 s period. We then use the direct surface-wave tomographic method with period-dependent ray tracing to invert group and phase dispersion travel-time data simultaneously for three-dimensional (3D) shear-wave velocity (V_s) structure. The V_s model shows clear correlation with the known geologic features. The TFZ is associated with a high-velocity anomaly zone in the shallow crust, corresponding to metamorphic rocks due to magma intrusion. Low-velocity anomaly zones are mainly located to the west of the TFZ, caused by thick sedimentary layers in the Hefei Basin. Our study shows that, with ambient noise data recorded on a dense array and an advanced surface-wave inversion method, we can image detailed structure around the fault zone.

Key words: Tanlu fault zone, magma intrusion, ambient noise tomography, dense seismic array, direct surface-wave tomography.

1. Introduction

Ambient noise tomography (ANT) has emerged as one of the powerful geophysical methods to study Earth structures at different scales over the last ∼ 15 years. It is capable of turning seismic "noise" into useful signals to retrieve surface waves between stations based on cross-correlation and stacking analysis of ambient noise. The retrieved surface waves can then be used to invert high-resolution images of structures in the crust and upper mantle. Since the first ambient noise tomographic images of Rayleigh wave group velocity for southern California (Sabra et al. 2005; Shapiro et al. 2005), this method has been applied successfully around the world to image high-resolution crustal structures, including at regional scales in the Tibetan Plateau (Yao et al. 2006, 2008), the western USA (Moschetti et al. 2007; Lin et al. 2008; Yang et al. 2008b), the Iberian Peninsula (Villasenor et al. 2007), Southern Africa (Yang et al. 2008a), Southern Korea (Cho et al. 2007), Japan (Nishida et al. 2008), and New Zealand (Lin et al. 2007) and at continental scales across Europe (Yang et al. 2007), Australia (Saygin and Kennett 2010), China (Zheng et al. 2008), and the USA (Bensen et al. 2008; Liang and Langston 2008; Lin et al. 2008) as well as other places.

Recently, ANT has been combined with local dense seismic arrays to image high-resolution structures of the shallow crust (e.g. Lin et al. 2013; Roux et al. 2016; Liu and Ben-Zion 2017). This method is not limited by the temporal and spatial distribution of seismic events and has thus become an important method for studying shallow structures (Li et al. 2016; Zhang et al. 2016; Liu et al. 2018).

In this study, we aim to apply the ANT method to image the detailed structure of the Tanlu fault zone (TFZ) in the shallow crust based on a local dense array, which is located near Chao Lake, to the southeast of Hefei City, eastern China. The TFZ

[1] Laboratory of Seismology and Physics of Earth's Interior, School of Earth and Space Sciences, University of Science and Technology of China, Hefei 230026, Anhui, China. E-mail: zhang11@ustc.edu.cn

[2] Geological Exploration Technology Institute of Anhui Province, Hefei, Anhui, China.

[3] Anhui Institute of Geological Survey, Hefei, Anhui, China.

[4] National Geophysical Observatory at Mengcheng, University of Science and Technology of China, Hefei 230026, Anhui, China.

strikes for a length of 2400 km of sinistral displacement in China, being one of the largest continental strike-slip faults in the world. It is regarded as an important mid-Cenozoic magmatic activity belt, metallogenic belt, as well as seismic belt in eastern China. According to structural and geochronological studies, the TFZ can be subdivided into southern (in Jiangsu and Anhui Provinces), middle (from Shandong Province to Shenyang in Liaoning Province), and northern (from Shenyang in Liaoning Province to Zhaoxing in Heilongjiang Province) segments (Deng et al. 2013; Zhang et al. 2007). The northern segment is closely related to the subduction of the western Pacific Plate (Xu and Zhu 1994; Zhang et al. 2007; Zhao et al. 2016), while the middle and southern segments are related to the subduction of the South China Plate to the North China Plate (Okay and Celal Sengör 1992; Yin and Nie 1993; Li 1994; Gilder et al. 1999; Wang et al. 2003; Zhu et al. 2009; Zhao et al. 2016). Overall, the middle and southern segments of the TFZ show the characteristics of vertical strike-slip fault.

Due to its complicated crustal structure, strong tectonic activity, and seismic activity, many studies have focused on the southern segment of the TFZ, including seismic tomography studies for determining crustal velocity structure (Ma et al. 1991; Dong et al. 1998; Yang et al. 1999a, b; Liu et al. 2009, 2015; Huang et al. 2011), fault activity studies for determining how the activity of the fault varies along the strike (Shi et al. 2003; Xu et al. 2014), electromagnetic studies for determining electrical structure (Xiao et al. 2009; Zhang et al. 2010), and integrated geophysical studies (Wang et al. 1995; Hao et al. 2004). However, the detailed structure of the southern segment of TFZ in the shallow crust is still scarcely studied.

In this study, we present the detailed structure of the TFZ near Chao Lake to the southeast of Hefei, eastern China, by applying a new direct surface-wave tomography method using the surface-wave dispersion data extracted from continuously recorded ambient noise on a local dense array. Compared with the traditional ANT method, the direct surface-wave tomography method considers ray-bending effects on surface-wave tomography in the shallow complex medium. This is the first time that a local dense

seismic array has been used to characterize the shallow structure of the TFZ.

2. Ambient Noise Data Analysis

We deployed 53 short-period (5 s–100 Hz) QS-5A seismic stations around the TFZ to the southeast of Hefei, the capital city of Anhui Province. The temporary array continuously recorded the data for about 1 month from 17 March to 26 April 2017. The seismic array spans an area of about 30 km × 40 km with average station spacing of about 5 km (Fig. 1). The vertical component data were used for ANT in this study.

Following the standard ambient noise processing procedure (Bensen et al. 2007), the vertical component data were first decimated at a sampling rate of 50 Hz. We then removed the mean and trend of the data, and band-pass filtered the data in the frequency band of 0.2–10 s. To suppress the effects of earthquakes, we also performed spectral whitening and multiple-band temporal normalization on the data (Zhang et al. 2018). After these steps, we performed time-domain ambient noise cross-correlation between two stations for each hourly data with lag time from −60 to 60 s. All the hourly cross-correlation functions (CCFs) from each station pair were stacked by using normalized linear stacking method. The time-domain empirical Green's function was then derived from the time derivative of the CCFs (Sabra et al. 2005; Yao et al. 2006). We can observe the emergence of surface-wave signals (Fig. 2a) from cross-correlation functions with signal-to-noise ratio (SNR) greater than five in the 0.2–5 s period band. Here, the SNR is defined as the ratio of the maximum amplitude of the signal window of CCFs (−30 to ∼ 30 s) and the average absolute amplitude of the noise window (−60 to ∼ −30 s and 30 to ∼ 60 s). To check the azimuthal distribution of ambient noise sources, we compute the relative amplitude ratios of the positive- and negative-time CCFs for all station pairs. Most values of relative amplitude ratios are between 0.5 to 1.5 (Fig. 2b), which means there are small amplitude differences between positive- and negative-time CCFs. Thus, we can deduce that the noise source distribution does not have significant
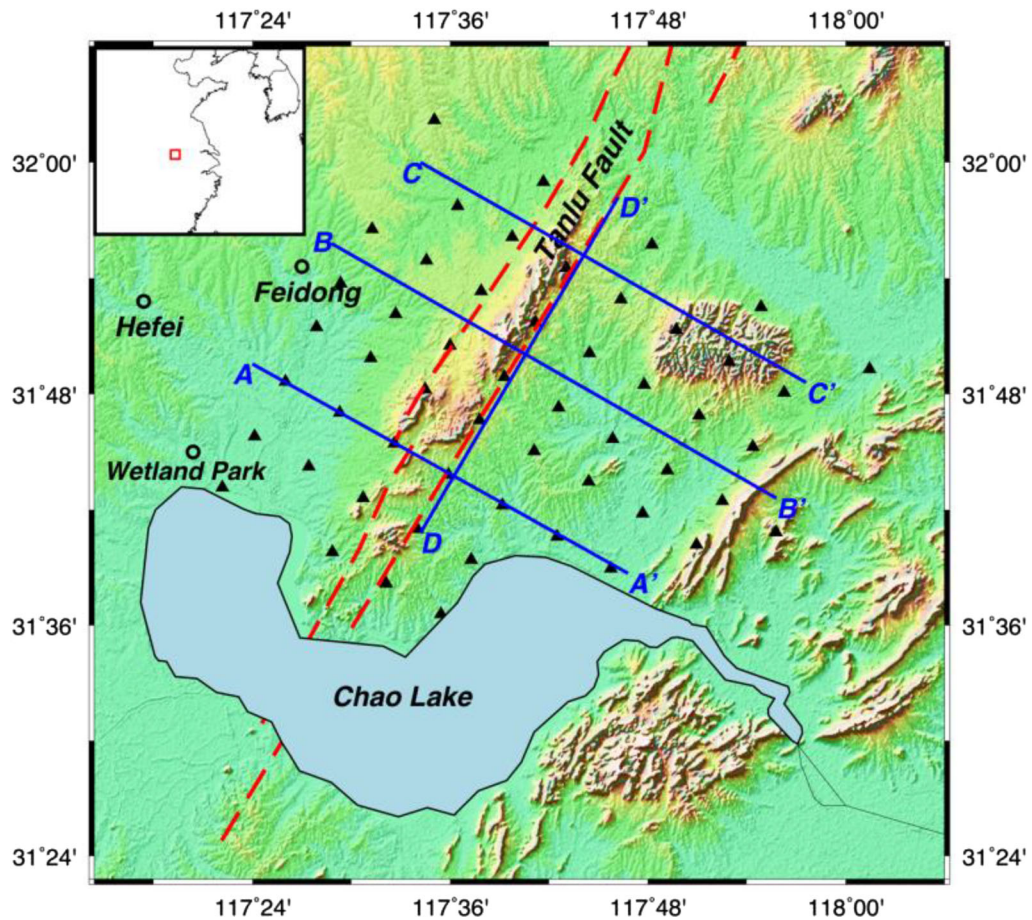
Figure 1

Distribution of seismic array stations (black triangles) and TFZ (red dashed lines) near Chao Lake located to the southeast of Hefei City. Red square in the upper-left inset shows the location of the survey. The blue lines marked by AA', BB', CC', and DD' represent the profiles shown in Fig. 11

azimuthal variations, which will not cause large bias in dispersion measurements (Yao and Van der Hilst 2009). For this reason, we can expect the noise sources to be generally distributed randomly. After stacking the positive-time and negative-time parts linearly, we used the image analysis method by Yao et al. (2006, 2011) to extract the fundamental mode Rayleigh wave group and phase velocity dispersion curves.

Figure 3a and b show all the group and phase velocity dispersion curves for the period range of 0.2–5 s for the fundamental mode Rayleigh waves, respectively. The quantity of dispersion data decreases with increasing period. Above the 5 s period, no measurements can be made due to relatively short

interstation distance. The velocity variation in the study region appears to be very large, as inferred from the dispersion curves; For example, at the period of 0.5 s, group velocity varies from 0.7 to 3 km/s and phase velocity changes from 0.8 to 2.9 km/s. In total, we obtained 482 dispersion data, including 246 group velocity measurements and 236 phase velocity measurements.

3. Direct Surface Wave Tomography of 3D V_s Model

We used a direct surface-wave tomography method (DSurfTomo) to simultaneously invert group and phase velocity dispersion data for the 3D shear
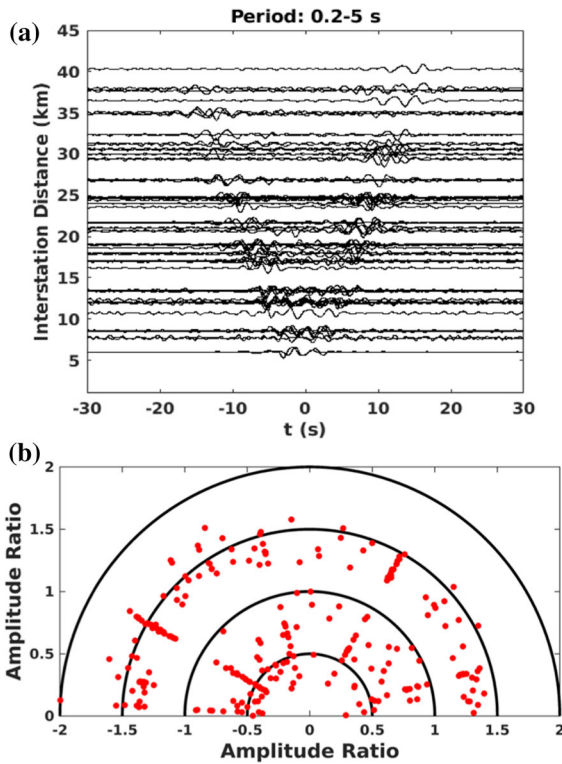
Figure 2

a Cross-correlation functions (CCFs) with signal-to-noise ratio (SNR) greater than five in the 0.2–5 s period band obtained from normalized linear stacking method. **b** Azimuthal distribution of the amplitude ratio (red dots) between the maximum envelope amplitudes of the positive-time and negative-time parts of CCFs in **a**. The azimuth of each red dot gives the azimuth direction of each station pair. Some relative amplitude ratios are linearly distributed, caused by the linear distribution of stations (Fig. 1)
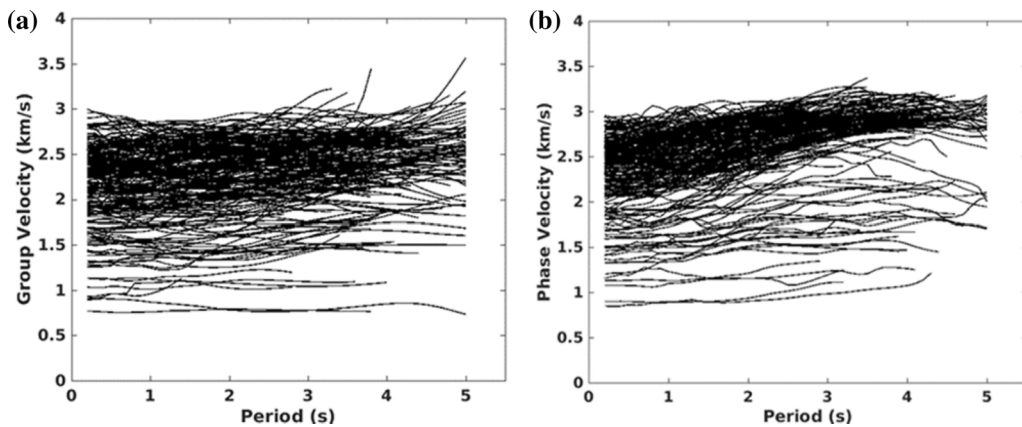
velocity structure (Fang et al. 2015). This method avoids the intermediate step of inversion for group or phase velocity maps. Importantly, it considers ray-bending effects of surface waves due to complicated velocity structure based on the fast-marching method (Rawlinson and Sambridge 2004). The travel-time perturbation at angular frequency ω with respect to a reference model for path **i** is given by

$$\delta t_i(\omega) = t_i^{\text{obs}} - t_i(\omega) \approx - \sum_{k=1}^{K} v_{ik} \frac{\delta C_k(\omega)}{C_k^2(\omega)}, \qquad (1)$$

where $t_i^{\text{obs}}(\omega)$ is the observed surface-wave travel time, $t_i(\omega)$ is the calculated travel time from a reference model which can be updated in the inversion, and v_{ik} are the bilinear interpolation coefficients along the ray path associated with the **i**th travel-time data, the phase or group velocity $C_k(\omega)$ and its perturbation $\delta C_k(\omega)$ at the **k**th two-dimensional (2D) surface grid point at angular frequency ω. For one-dimensional (1D) depth kernels of Rayleigh wave phase or group velocity data with respect to compressional velocity and density at each surface grid node, they are converted with respect to shear velocity with the scaling factor $R_\alpha(z_j)$ and $R_\rho(z_j)$ derived from the empirical relationship of Brocher (2005) (see Fang et al. 2015). Thus, Eq. (1) can be rewritten as (Fang et al. 2015)

Figure 3

a Group velocity and **b** phase velocity dispersion curves in the 0.2–5 s period band
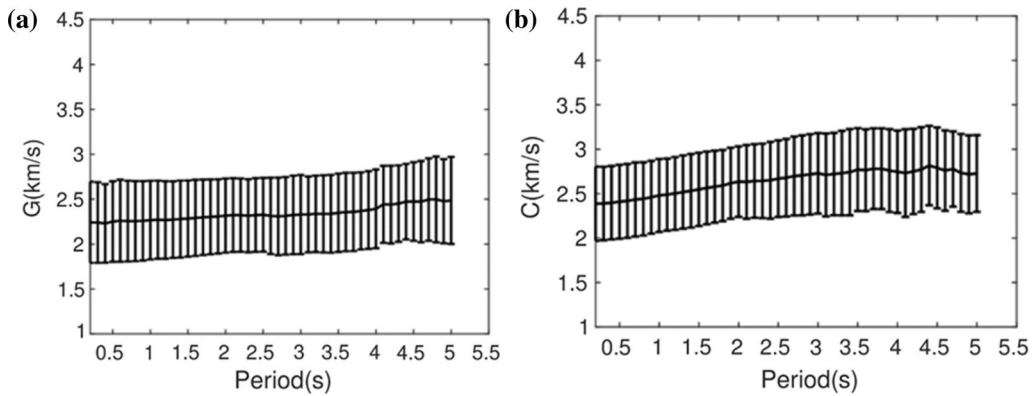
(a)

(b)

Figure 4
Average **a** group dispersion curve and **b** phase dispersion curve. Black bars represent standard deviations

$$\delta t_i(\omega) = \sum_{k=1}^{K} \left(-\frac{v_{ik}}{C_k^2} \right)$$
$$\sum_{j=1}^{J} \left[R'_\alpha(z_j) \frac{\partial C_k}{\partial \alpha_k(z_j)} + R'_\rho(z_j) \frac{\partial C_k}{\partial \rho_k(z_j)} + \frac{\partial C_k}{\partial \beta_k(z_j)} \right] \Bigg|_{\theta_k}$$
$$\delta \beta_k(z_j) = \sum_{l=1}^{M} G_{il} m_l,$$
$$(2)$$

where θ_k represents the 1D reference model at the **k**th surface grid point on the surface and $\alpha_k(z_j)$, $\beta_k(z_j)$, and $\rho_k(z_j)$ are the compressional velocity, shear velocity, and mass density at the jth node in the depth direction, respectively, and $M = KJ$, which is the total number of grid points of the 3D model.

The direct surface-wave tomography Eq. (2) can be further formulated into matrix form as

$$\mathbf{d} = \mathbf{Gm}, \qquad (3)$$

where $\mathbf{d}$ is the surface-wave travel-time residual vector for all ray paths at different periods, $\mathbf{G}$ is the data sensitivity matrix, and $\mathbf{m}$ is the model parameter vector. To make the inversion stable, both damping and first-order smoothing regularizations are applied.

4. Inversion Details and Model Resolution Tests

In general, the selection of the initial model is important for linearized inversion. To determine an optimal 1D shear-wave velocity model, we used the average group and phase velocity dispersion curves

for the study region (Fig. 4). An average 1D model is then determined by using the average dispersion curves, which is used as the initial model for the direct 3D surface-wave tomography (Fig. 5).

We first check the depth sensitivities of the surface-wave phase velocity and group velocity at different periods with respect to the compressional velocity, shear velocity, and density. At a given frequency f, the depth sensitivity kernels of phase velocity can be written as

$$\frac{\delta C(f)}{C(f)} = \int_0^R \left\{ K_\alpha(f) \frac{\delta \alpha}{\alpha} + K_\beta(f) + K_\rho(f) \frac{\delta \rho}{\alpha \rho} \right\} dz,$$
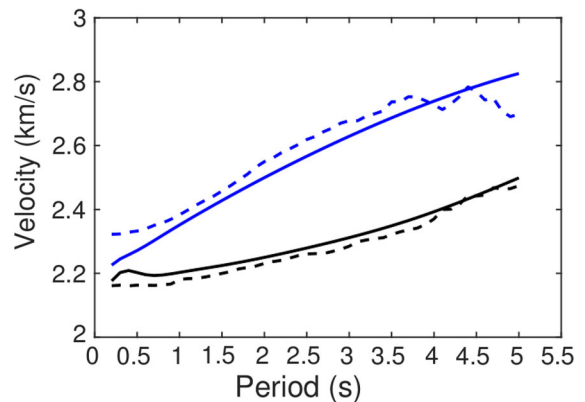$$(4)$$

Figure 5
Observed and synthetic group and phase velocity dispersion curves. The blue dashed line represents the average phase dispersion curve, and the blue solid line represents the synthetic phase dispersion curve. The black dashed and solid line represent the average and the synthetic group dispersion curves, respectively
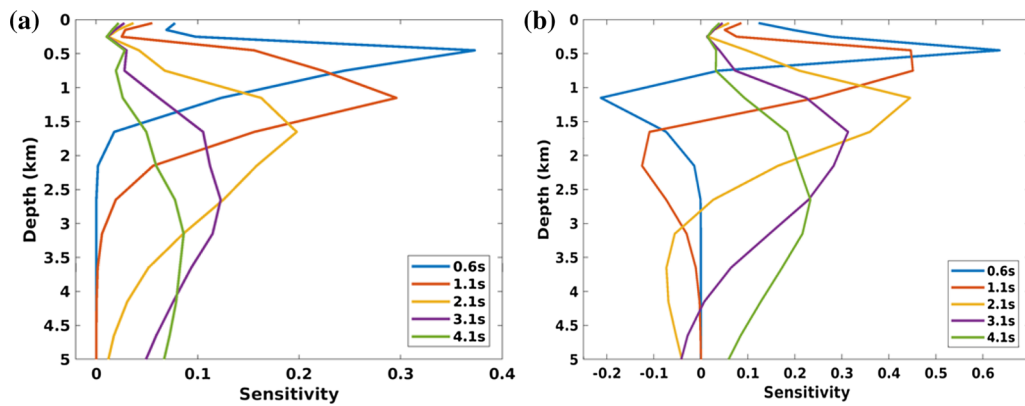
Figure 6
Depth sensitivity kernels for **a** phase velocity and **b** group velocity at five periods (0.6 s, 1.1 s, 2.1 s, 3.1 s, and 4.1 s)
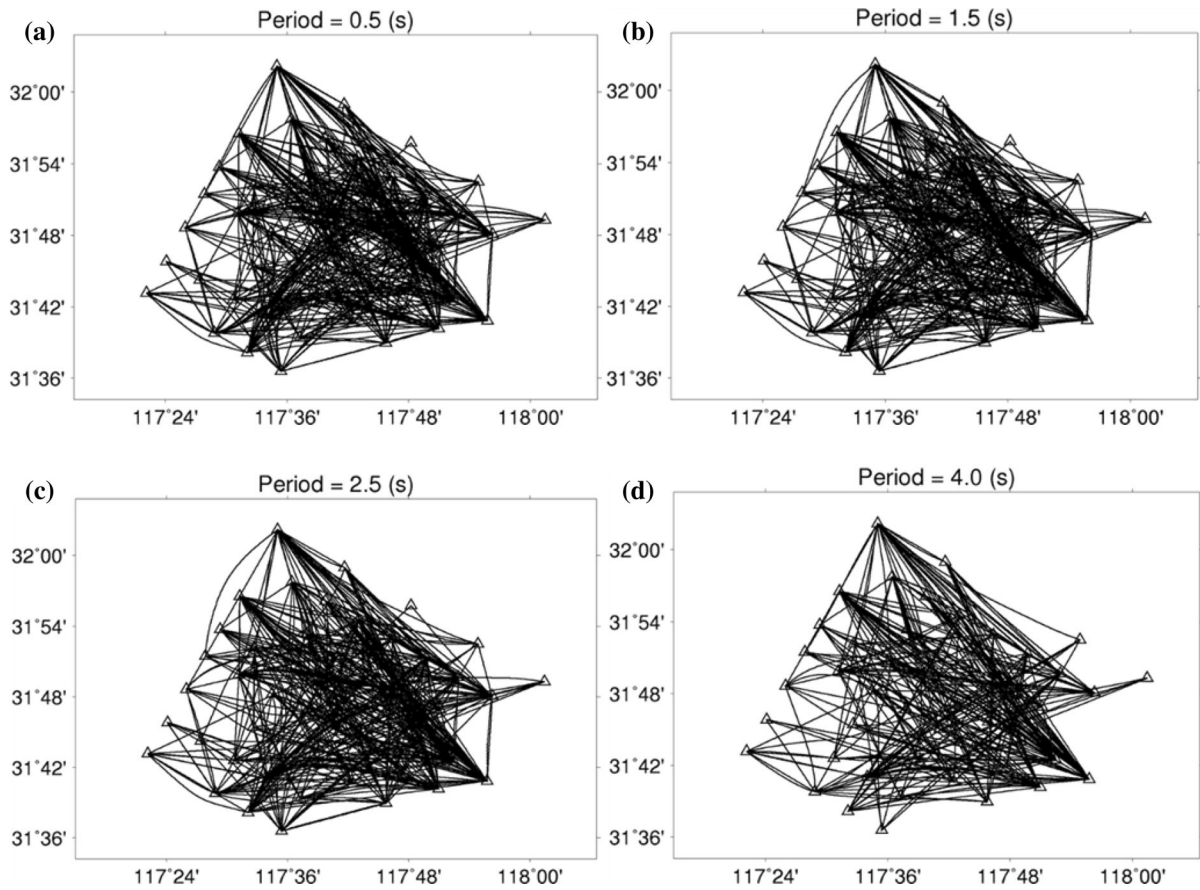

Figure 7
Ray-path coverage for four selected periods: **a** 0.5 s, **b** 1.5 s, **c** 2.5 s, and **d** 4.0 s. Triangles represent stations, and black lines represent ray paths
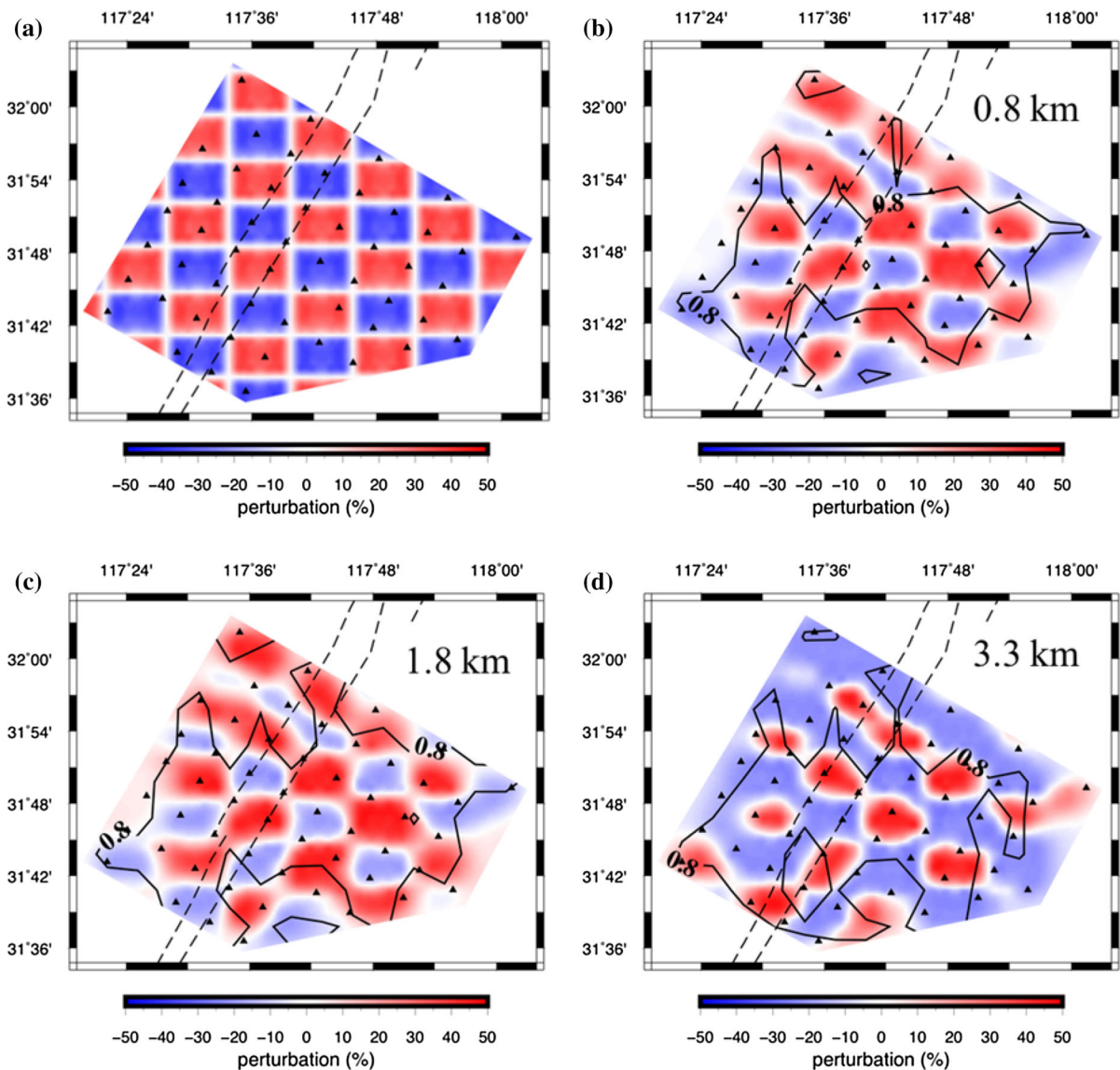
Figure 8
Checkerboard resolution tests of the inversion. **a** The input checkerboard model and **b–d** the recovered checkerboard models at depths of 0.8, 1.8, and 3.3 km, respectively. The black dashed lines represent TFZ. The black contour shows the semblance value of 0.8 between true and recovered checkerboard models

where z represents the depth, C is the Rayleigh wave group or phase velocity, and $K_\alpha(f)$, $K_\beta(f)$, and $K_\rho(f)$ are the depth sensitivity kernels for Rayleigh wave group or phase velocity to α, β, and ρ, respectively. Figure 6a, b show the depth sensitivity kernels for Rayleigh wave group and phase velocities at five periods (0.6, 1.1, 2.1, 3.1, and 4.1 s), using the average 1D velocity model obtained for the study

area. It can be seen that, at the period of 0.6 s, the data have some sensitivity to the structure shallower than 400 m depth. At about 3.1 s, our dispersion data can have good sensitivity to structures around 3 km in depth. It can be seen that the surface-wave dispersion data between 0.2 and 5 s have the ability to resolve at depth down to 5 km. It can also be seen that the sensitivity kernels for the phase velocity and

group velocity are complementary at the same frequency. As a result, we simultaneously use both phase velocity and group velocity dispersion curves for joint inversion.

For the inversion grid, the grid spacing is 0.015° along the north–south direction and 0.025° along the east–west direction, thus giving $40 \times 40 = 1600$ horizontal grid points. We set 15 grid points (at 0, 0.1, 0.2, 0.3, 0.5, 0.8, 1.3, 1.8, 2.3, 2.8, 3.3, 3.8, 4.3, 4.8, and 5.3 km) along the depth direction from surface to 5.3 km, with larger grid spacing at deeper region. The inversion grid is selected by trial and error to ensure the model is fine enough but at the same time can be well resolved under the current data distribution through resolution tests. To evaluate the model resolution, we first check the surface-wave path coverage at different periods and then conduct checkerboard resolution test.

Figure 7 shows the path coverage of phase velocity measurements at the four selected periods (0.5, 1.5, 2.5, and 4.0 s) based on the final 3D velocity model. The path number decreases from 235 at the 0.5 s period to 154 at the 4.0 s period. It can be seen that, at these periods, the ray coverage is relatively good, indicating that this dataset has the ability to resolve the structure of the study region. To further evaluate the spatial resolution of the inversion model at different depths, we performed checkerboard resolution tests with the input anomalies following a sine function, and the amplitude range varies from −50 to 50 % of the average velocity at each depth. Each anomaly has a size of 5 km in the north–south direction and 6 km in the east–west direction. Figure 8 shows the recovered checkerboard models at different depths with the same path distribution as the real data. It can be seen that checkerboard models are recovered well in the central part of the study region where the ray coverage is dense (Fig. 8).

To quantitatively measure the similarity between input and recovered checkerboard models, we calculate the semblance (S) between two models (Neidell and Taner 1971):

$$S = \frac{(dV_r + dV_t)^2}{2(dV_r^2 + dV_t^2)}, \qquad (5)$$

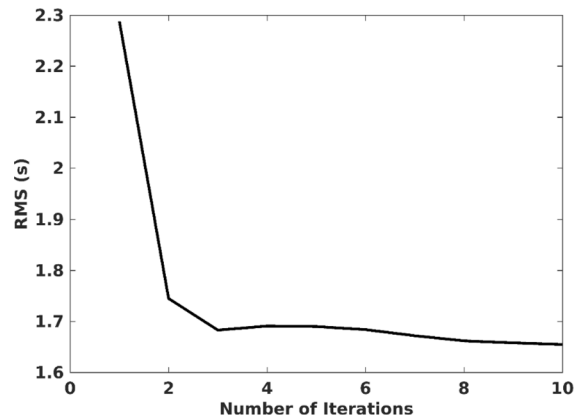where dV_t and dV_r are V_s perturbations of true and recovered checkerboard models, respectively.

Figure 9
Variation of the RMS value of surface-wave travel-time residuals through the iterations

S denotes the similarity between recovered and true models, being closer to 1 if the two models are similar. We incorporate the contour value of 0.8 for semblance into the recovered checkerboard models (Fig. 8). It shows that the central part of the study region is within the 0.8 contour value of semblance, indicating that the checkerboard model is well recovered. This test suggests that the velocity anomalies in most of the inversion region can be well resolved due to relatively dense data coverage.

For the inversion, we carefully selected regularization parameters through trade-off analysis (Aster et al. 2013). After inversion, the root-mean-square (RMS) value of surface-wave travel-time residuals decreases from about 2.3 s to about 1.65 s (Fig. 9). It can be seen that the RMS value of travel-time residuals decreases quickly in the first three iterations. After that, the RMS residual value decreases slowly and converges after the 10th iteration.

5. Results and Discussion

Figure 10 shows the V_s model at different depths from the joint inversion of group and phase velocity dispersion data. Figure 11 shows the cross-sections of

Figure 10   ▶
Map view of the V_s model at depths of 0.2, 0.5, 1.3, 1.8, 2.3, 2.8, 3.3, and 3.8 km. Black triangles represent stations. Dashed line shows the TFZ
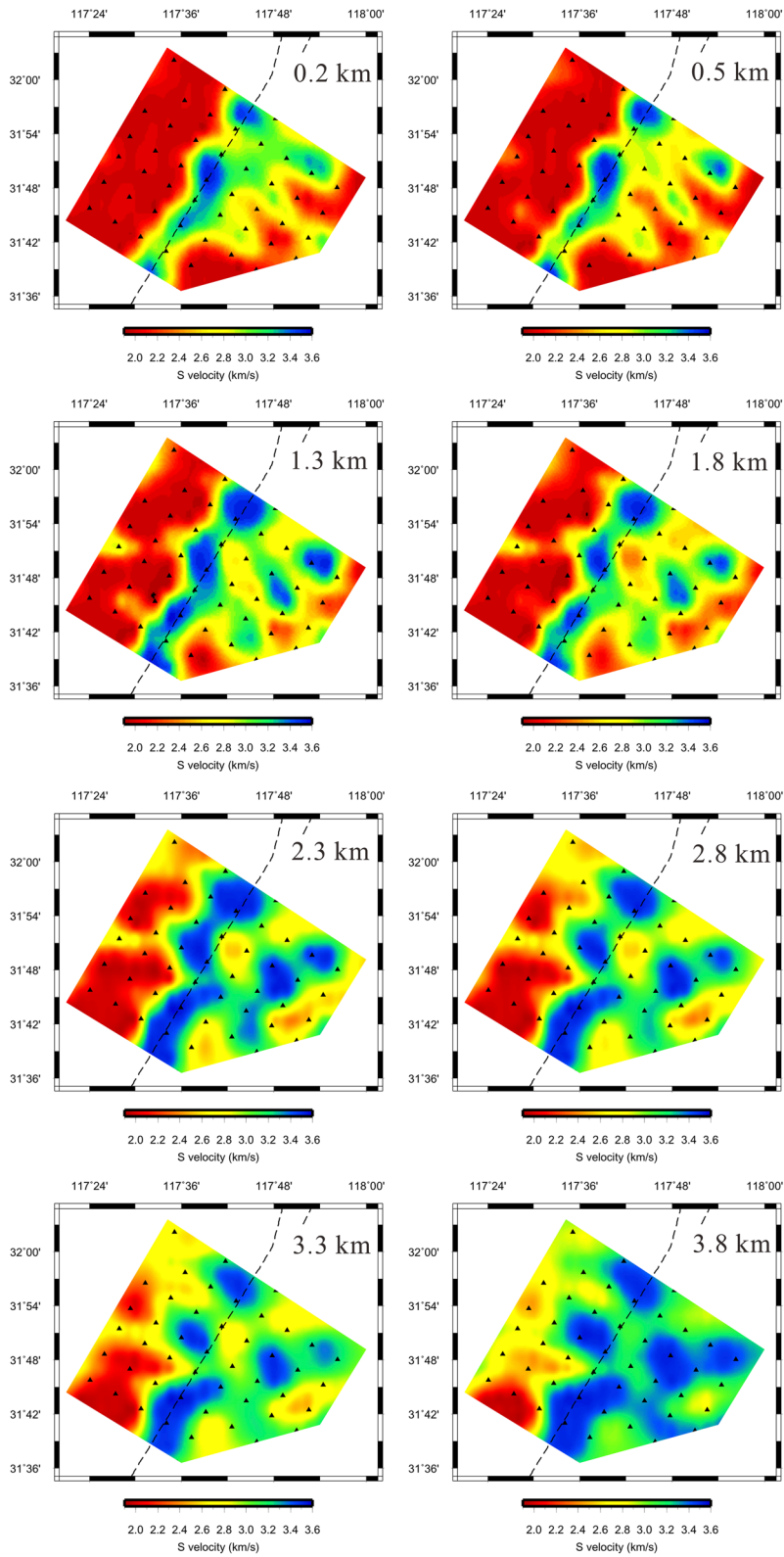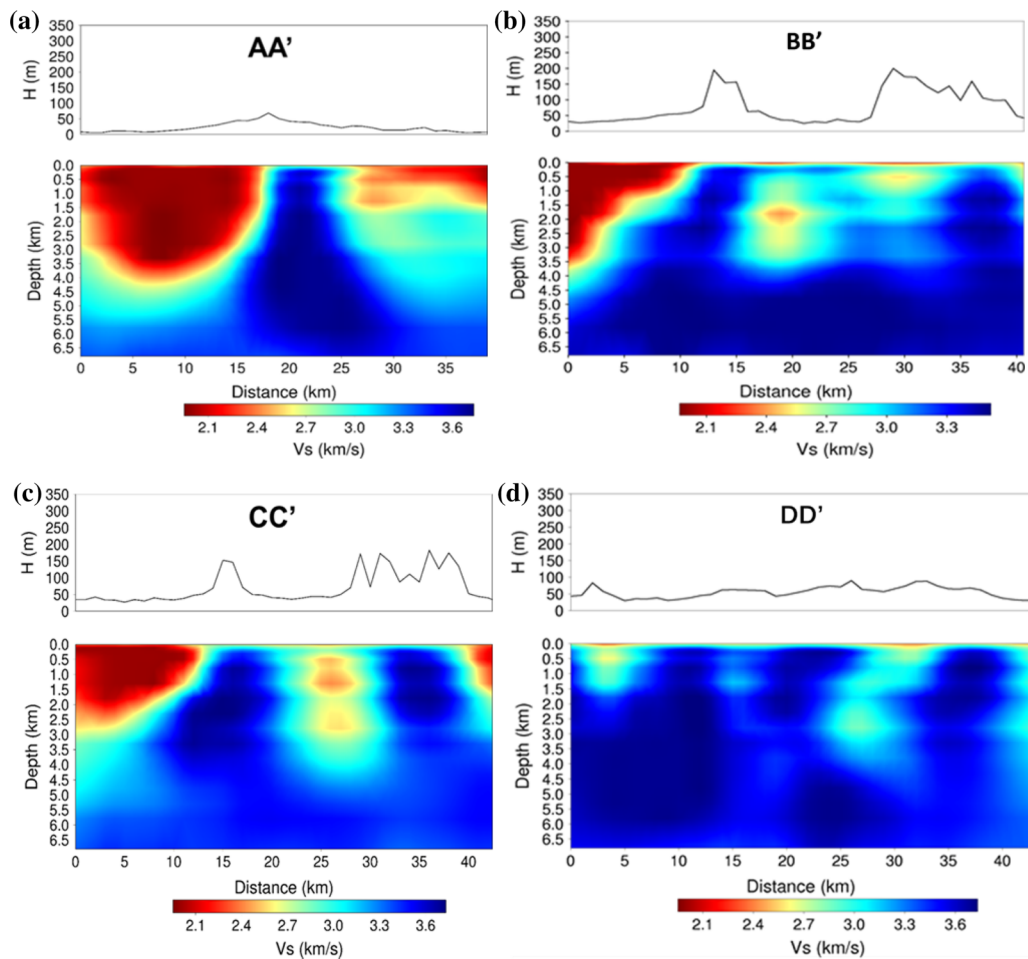
Figure 11
Cross-sections of the V_s model along AA', BB', CC', and DD'. In **a–d**, topography variations are shown along the profile

the V_s model through four profiles shown in Fig. 1. The V_s model shows that the velocity varies significantly in the study region, consistent with the dispersion curve pattern seen in Fig. 3. Because of large velocity variations, the surface-wave ray paths at different periods significantly bend off the great-circle paths (Fig. 7).

It can be seen that the TFZ is associated with high-velocity anomalies down to ~ 6 km in depth (Figs. 10, 11). Along the profiles AA', BB', and CC', the velocity changes sharply across the TFZ (Fig. 11). It can be seen that the western edge of the TFZ has different dipping angle from north to south. In the southern part it is steeper, while in the northern part it is gradual. In the map view, it can be seen that

the TFZ is bent in the center and the offset is about 10 km (Fig. 10). The checkerboard test shows that the offset of 10 km can be resolved by the current data distribution. This bent shape can be clearly seen at the depth of 2.3 km (Fig. 10). It can also be seen that high-velocity anomalies associated with the TFZ are not continuous at different depths.

The TFZ is also associated with high-gravity (Fig. 12a) and high-magnetic (Fig. 12b) anomalies. On the surface, metamorphic rocks are exposed along the TFZ. Therefore, high-velocity anomalies imaged along the TFZ down to ~ 6 km can be interpreted as metamorphic rocks. This indicates that the TFZ in this segment may serve as channels for magma intrusion. According to Niu et al. (2005), large basalt
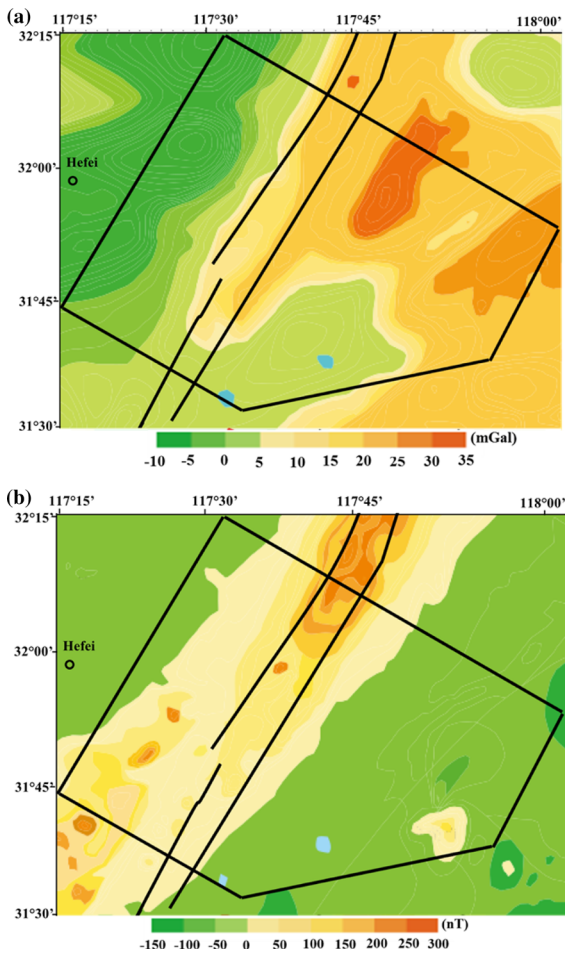
Figure 12

a Bouguer gravity and **b** aeromagnetic anomalies. Black lines represent the TFZ. Black box shows the study area

eruptions occurred in the Cenozoic era during the evolution of the TFZ. It was thought that the TFZ could cut into the upper mantle during the strong Pleistocene extension, and thus could constitute the channel for the basalt eruption (Niu et al. 2005; Zhu et al. 2001a, b). Our ambient noise tomography V_s model in the shallow crust for the first time provides direct evidence supporting this hypothesis.

To the northwest of the TFZ, low velocity anomalies reach down to ~ 3.5 km, especially at the southwest corner of the study region (Figs. 10, 11). They correspond to sedimentary layers in the Hefei basin. Evidently, the low velocity anomaly zone goes deeper in the southwest corner of the study region (Fig. 10), which is close to Chao Lake and is

associated with the Hefei Binhu wetland park. The low velocity anomalies to the west of the TFZ are associated with low gravity anomalies. To the east of the TFZ, it is mainly composed of old strata of the Qingbaikou, Sinian, and Cambrian (Zhu et al. 2001a, b; Niu et al. 2005; Wang et al. 2016). The shear-wave velocity varies from ~ 2.5 to 3.0 km/s. About 20 km farther from the TFZ, there is an obvious high-velocity anomaly zone starting from depth of 1.5 km. It also corresponds to high-gravity anomalies but normal magnetic anomalies (Fig. 12). This indicates that this high-velocity anomaly zone may have different origins from the high-velocity zone along the TFZ.

We also compared our velocity model with a known geological profile along profile BB' (Fig. 13). Although the overall features are similar between the geophysical and geological profiles, there are apparent inconsistencies between them; For example, our high-resolution velocity result shows that the western edge of the TFZ dips gently, while the geological mapping gives a sharper edge. This indicates that ambient noise tomography using a local dense array can be very useful for depicting an accurate geological profile.

6. Conclusions

We applied direct surface-wave tomography using 1 month of ambient noise data recorded by a local dense array to investigate the structure of TFZ to the southeast of Hefei City, China. We are able to extract Rayleigh wave group and phase velocity dispersion curves for periods of 0.2–5 s. A high-resolution 3D shear-wave velocity structure shows high-velocity anomalies beneath the TFZ, which is consistent with locally high-gravity and high-magnetic anomalies. They are associated with metamorphosed rocks exposed on the surface, likely caused by magma intrusion via the TFZ. The Hefei basin is characterized by low velocity anomalies down to ~ 3.5 km due to thick sedimentary layers. Overall, our results agree well with the local geology and can provide strong constraints on geological modeling in this region.
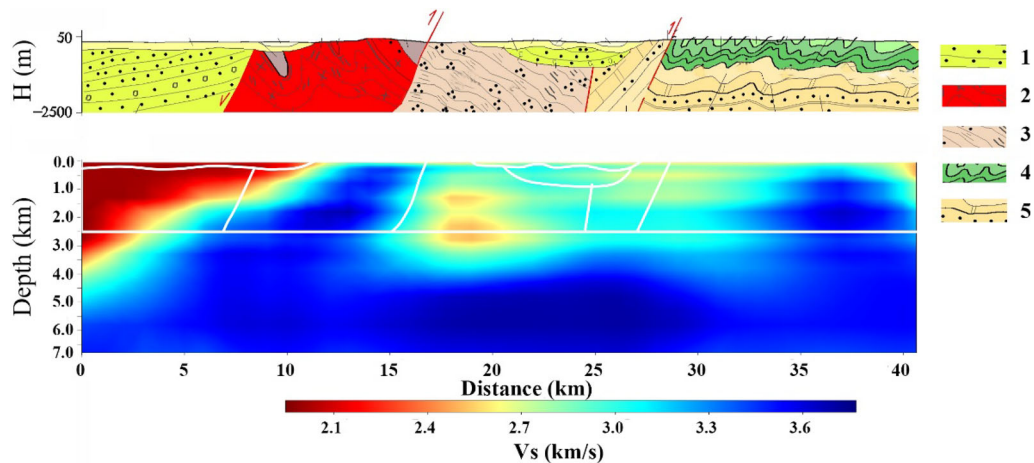
Figure 13
Local geological section along the same *S* wave velocity profile *BB′* in Fig. 9. White lines represent different stratigraphic units by geological mapping. 1 = Upper Cretaceous sandstone; 2 = Paleoproterozoic gneiss; 3 = Qingbaikou Period limestone; 4 = Early Cambrian shale; 5 = Sinian limestone

REFERENCES

Aster, R. C., Borchers, B., & Thurber, C. H. (2013). *Parameter estimation and inverse problems* (2nd ed.). Academic Press.

Bensen, G. D., Ritzwoller, M. H., Barmin, M. P., Levshin, A. L., Lin, F., Moschetti, M. P., et al. (2007). Processing seismic ambient noise data to obtain reliable broad-band surface wave dispersion measurements. *Geophysical Journal International, 169*(3), 1239–1260.

Bensen, G. D., Ritzwoller, M. H., & Shapiro, N. M. (2008). Broadband ambient noise surface wave tomography across the United States. *Journal of Geophysical Research: Solid Earth, 113*, B05306. https://doi.org/10.1029/2007JB005248.

Brocher, T. M. (2005). Empirical relations between elastic wave-speeds and density in the Earth's crust. *Bulletin of the Seismological Society of America, 95*(6), 2081–2092.

Cho, K. H., Herrmann, R. B., Ammon, C. J., & Lee, K. (2007). Imaging the upper crust of the Korean Peninsula by surface-wave tomography. *Bulletin of the Seismological Society of America, 97*(1B), 198–207.

Deng, Y., Fan, W., Zhang, Z., & Badal, J. (2013). Geophysical evidence on segmentation of the Tancheng-Lujiang fault and its implications on the lithosphere evolution in East China. *Journal of Asian Earth Sciences, 78*, 263–276.

Dong, S. W., Wu, X. Z., Gao, R., Lu, D. Y., Li, Y. K., He, Y. Q., et al. (1998). On the crust velocity levels and dynamics of the Dabieshan orogenic belt. *Acta Geophysica Sinica, 41*, 361–369.

Fang, H., Yao, H., Zhang, H., Huang, Y. C., & van der Hilst, R. D. (2015). Direct inversion of surface wave dispersion for three-dimensional shallow crustal structure based on ray tracing: Methodology and application. *Geophysical Journal International, 201*(3), 1251–1263.

Gilder, S. A., Leloup, P. H., Courtillot, V., Chen, Y., Coe, R. S., Zhao, X., et al. (1999). Tectonic evolution of the Tancheng-Lujiang (Tan-Lu) fault via middle Triassic to Early Cenozoic paleomagnetic data. *Journal of Geophysical Research: Solid Earth, 104*(B7), 15365–15390.

Hao, T. Y., Suh, M., & Liu, J. H. (2004). Deep structure and boundary belt position between Sino-Korean and Yangtze blocks in Yellow Sea. *Earth Science Frontiers, 11*, 51–62.

Huang, Y., Li, Q. H., Zhang, Y. S., Sun, Y. J., Bi, X. M., Jin, S. M., et al. (2011). Crustal velocity structure beneath the Shandong-Jiangsu-Anhui segment of the Tancheng-Lujiang fault zone and adjacent areas. *Chinese Journal of Geophysics (in Chinese), 54*(10), 2549–2559. https://doi.org/10.3969/j.issn.0001-5733.2011.10.012.

Li, Z.-X. (1994). Collision between the North and South China blocks: A crustal-detachment model for suturing in the region east of the Tanlu fault. *Geology, 22*(8), 739–742.

Li, C., Yao, H., Fang, H., Huang, X., Wan, K., Zhang, H., et al. (2016). 3D near-surface shear-wave velocity structure from ambient-noise tomography and borehole data in the Hefei urban area, China. *Seismological Research Letters, 87*(4), 882–892.

Liang, C., & Langston, C. A. (2008). Ambient seismic noise tomography and structure of eastern North America. *Journal of*

Geophysical Research: Solid Earth, 113, B03309. https://doi.org/10.1029/2007JB005350.

Lin, F. C., Moschetti, M. P., & Ritzwoller, M. H. (2008). Surface wave tomography of the western United States from ambient seismic noise: Rayleigh and Love wave phase velocity maps. *Geophysical Journal International, 173*(1), 281–298.

Lin, F. C., Ritzwoller, M. H., Townend, J., Bannister, S., & Savage, M. K. (2007). Ambient noise Rayleigh wave tomography of New Zealand. *Geophysical Journal International, 170*(2), 649–666.

Lin, F. C., Li, D., Clayton, R. W., & Hollis, D. (2013). High-resolution 3D shallow crustal structure in Long Beach, California: application of ambient noise tomography on a dense seismic arrayNoise tomography with a dense array. *Geophysics*, 78(4), Q45–Q56.

Liu, X., & Ben-Zion, Y. (2017). Analysis of non-diffuse characteristics of the seismic noise field in southern California based on correlations of neighbouring frequencies. *Geophysical Journal International, 212*(2), 798–806.

Liu, Y., Wang, Q., Jiang, M., & Wang, Y. J. (2009). The receiver function image of the deep structure in Sulu orogenic belt. *Acta Petrologica Sinica (in Chinese), 25*(7), 1658–1662.

Liu, Y., Zhang, H., Fang, H., Yao, H., & Gao, J. (2018). Ambient noise tomography of three-dimensional near-surface shear-wave velocity structure around the hydraulic fracturing site using surface microseismic monitoring array. *Journal of Applied Geophysics, 159,* 209–217.

Liu, B., Zhu, G., Zhang, M. J., Gu, C. C., Song, L. H., & Liu, S. (2015). Features and genesis of active faults in the Anhui segment of the Tan-Lu fault zone. *Chinese Journal of Geology (Scientia Geologica Sinica), 2,* 017.

Ma, X. Y., Liu, C. Q., & Liu, G. D. (1991). Xiangshui (Jiangsu Province) to Mandal (Nei Monggol) geoscience transect. *Acta Geologica Sinica, 3,* 199–215.

Moschetti, M. P., Ritzwoller, M. H., & Shapiro, N. M. (2007). Surface wave tomography of the western United States from ambient seismic noise: Rayleigh wave group velocity maps. *Geochemistry, Geophysics, Geosystems*, 8, Q08010. https://doi.org/10.1029/2007GC001655.

Neidell, N. S., & Taner, M. T. (1971). Semblance and other coherency measures for multichannel data. *Geophysics, 36*(3), 482–497.

Nishida, K., Kawakatsu, H., & Obara, K. (2008). Three-dimensional crustal wave velocity structure in Japan using microseismic data recorded by Hi-net tiltmeters. *Journal of Geophysical Research: Solid Earth*, 113, B10302. https://doi.org/10.1029/2007JB005395.

Niu, M. L., Zhu, G., Liu, G. S., Song, C. Z., & Wang, D. (2005). Cenozoic volcanic activities and deep processes in the middle-south sector of the Tan-Lu fault zone. *Chinese Journal of Geology, 40,* 390–403.

Okay, A. I., & Celal Şengör, A. M. (1992). Evidence for intra-continental thrust-related exhumation of the ultra-high-pressure rocks in China. *Geology, 20*(5), 411–414.

Rawlinson, N., & Sambridge, M. (2004). Wave front evolution in strongly heterogeneous layered media using the fast marching method. *Geophysical Journal International, 156*(3), 631–647.

Roux, P., Moreau, L., Lecointre, A., Hillers, G., Campillo, M., Ben-Zion, Y., et al. (2016). A methodological approach towards high-resolution surface wave imaging of the San Jacinto Fault Zone using ambient-noise recordings at a spatially dense array. *Geophysical Journal International, 206*(2), 980–992.

Sabra, K. G., Gerstoft, P., Roux, P., Kuperman, W. A., & Fehler, M. C. (2005). Surface wave tomography from microseisms in Southern California. *Geophysical Research Letters, 32*, L14311. https://doi.org/10.1029/2005GL023155.

Saygin, E., & Kennett, B. L. (2010). Ambient seismic noise tomography of Australian continent. *Tectonophysics, 481*(1–4), 116–125.

Shapiro, N. M., Campillo, M., Stehly, L., & Ritzwoller, M. H. (2005). High-resolution surface-wave tomography from ambient seismic noise. *Science, 307*(5715), 1615–1618.

Shi, W., Zhang, Y. Q., & Dong, S. W. (2003). Quaternary activity and segmentation behavior of the middle portion of the Tan-Lu fault zone. *Acta Geoscientia Sinica, 24*(1; ISSU 73), 11–18.

Villasenor, A., Yang, Y., Ritzwoller, M. H., & Gallart, J. (2007). Ambient noise surface wave tomography of the Iberian Peninsula: Implications for shallow seismic structure. *Geophysical Research Letters, 34*, L11304. https://doi.org/10.1029/2007GL030164.

Wang, L., Li, C., Shi, Y., & Wang, Y. (1995). Distributions of geotemperature and terrestrial heat flow density in lower Yangtze area. *Chinese Journal of Geophysics, 38*(04), 469–476.

Wang, E., Meng, Q., Burchfiel, B. C., & Zhang, G. (2003). Mesozoic large-scale lateral extrusion, rotation, and uplift of the Tongbai-Dabie Shan belt in east China. *Geology, 31*(4), 307–310.

Wang, W., Song, C., Ren, S., Li, J., Zhang, Y., Wang, P., et al. (2016). PT conditions and zircon U-Pb analysis of the Taoyuan ductile shear zone in Tan-Lu fault zone. *Acta Petrologica Sinica, 3,* 011.

Wessel, P., & Smith, W. H. (1995). New version of the generic mapping tools. *Eos, Transactions American Geophysical Union*, 76(33), 329–329.

Xiao, Q., Zhao, G., Wang, J., Zhan, Y., Chen, X., Tang, J., et al. (2009). Deep electrical structure of the Sulu orogen and neighboring areas. *Science in China, Series D: Earth Sciences, 52*(3), 420–430.

Xu, R., Chen, S. J., & Wang, F. (2014). Study on tectonic stress field in Yishu fault zone and its adjacent areas. *China Earthquake Engineering Journal (in Chinese), 36*(1), 158–169.

Xu, J. W., & Zhu, G. (1994). Tectonic models of the Tan-Lu fault zone, eastern China. *International Geology Review, 36*(8), 771–784.

Yang, W. C., Chen, Z. Y., Chen, G. J., Hu, Z. Y., & Bai, J. (1999a). Geophysical investigations in northern Sulu UHPM belt, Part I: Deep seismic reflection. *Chinese Journal of Geophysics-Chinese Edition, 42*(1), 41–52.

Yang, W. C., Hu, Z. Y., Cheng, Z. Y., Ni, C. C., Fang, H., & Bai, J. (1999b). Long profile of geophysical investigation from Tanchen to Lianshui, East-Central China. *Chinese Journal of Geophysics-Chinese Edition, 42*(2), 206–217.

Yang, Y., Li, A., & Ritzwoller, M. H. (2008a). Crustal and uppermost mantle structure in southern Africa revealed from ambient noise and teleseismic tomography. *Geophysical Journal International, 174*(1), 235–248.

Yang, Y., Ritzwoller, M. H., Levshin, A. L., & Shapiro, N. M. (2007). Ambient noise Rayleigh wave tomography across Europe. *Geophysical Journal International, 168*(1), 259–274.

Yang, Y., Ritzwoller, M. H., Lin, F. C., Moschetti, M. P., & Shapiro, N. M. (2008b). Structure of the crust and uppermost mantle beneath the western United States revealed by ambient noise and earthquake tomography. *Journal of Geophysical Research: Solid Earth, Earth,* 113(B12).

Yao, H., Beghein, C., & Van Der Hilst, R. D. (2008). Surface wave array tomography in SE Tibet from ambient seismic noise and two-station analysis—II. Crustal and upper-mantle structure. *Geophysical Journal International, 173*(1), 205–219.

Yao, H., Gouedard, P., Collins, J. A., McGuire, J. J., & van der Hilst, R. D. (2011). Structure of young East Pacific Rise lithosphere from ambient noise correlation analysis of fundamental- and higher-mode Scholte–Rayleigh waves. *Comptes Rendus Geoscience, 343*(8–9), 571–583.

Yao, H., & Van Der Hilst, R. D. (2009). Analysis of ambient noise energy distribution and phase velocity bias in ambient noise tomography, with application to SE Tibet. *Geophysical Journal International, 179*(2), 1113–1132.

Yao, H., van Der Hilst, R. D., & De Hoop, M. V. (2006). Surface-wave array tomography in SE Tibet from ambient seismic noise and two-station analysis—I. Phase velocity maps. *Geophysical Journal International, 166*(2), 732–744.

Yin, A., & Nie, S. (1993). An indentation model for the North and South China collision and the development of the Tan-Lu and Honam fault systems, eastern Asia. *Tectonics, 12*(4), 801–813.

Zhang, B. L., Li, Z. W., Bao, F., et al. (2016). Shallow shear-wave velocity structures under the Weishan volcanic cone in Wudalianchi volcano field by microtremor survey. *Chinese Journal of Geophysics (in Chinese), 59*(10), 3662–3673. https://doi.org/10.6038/cjg20161013.

Zhang, P., Wang, L. S., Zhong, K., & Ding, Z. Y. (2007). Research on the segmentation of Tancheng-Lujiang fault zone. *Geological Review, 53*(5), 586–591.

Zhang, Y., Yao, H., Yang, H. Y., Cai, H. T., Fang, H., Xu, J., et al. (2018). 3-D crustal shear-wave velocity structure of the Taiwan Strait and Fujian, SE China, revealed by ambient noise tomography. *Journal of Geophysical Research: Solid Earth, 123*(9), 8016–8031.

Zhang, J. H., Zhao, G. Z., Xiao, Q. B., & Tang, J. (2010). Analysis of electric structure of the central Tan-Lu fault zone (Yi-Shu fault zone, 36 N) and seismogenic condition. *Chinese Journal of Geophysics (in Chinese), 53*(3), 605–611.

Zhao, T., Zhu, G., Lin, S., & Wang, H. (2016). Indentation-induced tearing of a subducting continent: evidence from the Tan-Lu Fault Zone, East China. *Earth-Science Reviews, 152,* 14–36.

Zheng, S., Sun, X., Song, X., Yang, Y., & Ritzwoller, M. H. (2008). Surface wave tomography of China from ambient seismic noise correlation. *Geochemistry, Geophysics, Geosystems, 9*, Q05020. https://doi.org/10.1029/2008GC001981.

Zhu, G., Liu, G. S., Niu, M. L., Xie, C. L., Wang, Y. S., & Xiang, B. (2009). Syn-collisional transform faulting of the Tan-Lu fault zone, East China. *International Journal of Earth Sciences, 98*(1), 135–155.

Zhu, G., Song, C., Wang, D., Liu, G., & Xu, J. (2001a). Studies on 40 Ar/39 Ar thermochronology of strike-slip time of the Tan-Lu fault zone and their tectonic implications. *Science in China, Series D: Earth Sciences, 44*(11), 1002–1009.

Zhu, G., Wang, D. X., Liu, G. S., Song, C. Z., Xu, J. W., & Niu, M. L. (2001b). Extensional activities along the Tan-Lu fault zone and its geodynamic setting. *Chinese Journal of Geology, 36*(3), 269–278.